

Giant supercurrent drag effect between graphene and LaAlO₃/SrTiO₃ interface

Ran Tao^{1,2}, Lin Li^{1,2*}, Linhai Guo^{1,2}, Xiaodong Fan^{1,2}, Lijun Zhu^{1,2}, Yuedong Yan^{1,2}, Zhenyu Zhang¹, Changgan Zeng^{1,2*}

¹*International Center for Quantum Design of Functional Materials (ICQD), Hefei National Laboratory for Physical Sciences at the Microscale, and Synergetic Innovation Center of Quantum Information and Quantum Physics, University of Science and Technology of China, Hefei, Anhui 230026, China*

²*CAS Key Laboratory of Strongly-Coupled Quantum Matter Physics, and Department of Physics, University of Science and Technology of China, Hefei, Anhui 230026, China*

* Correspondence and requests for materials should be addressed to C. Z. (cgzeng@ustc.edu.cn), and L. L. (lilin@ustc.edu.cn).

Double-layer electronic systems enable the investigation of interlayer quasiparticle interactions¹ and the discovery of intriguing interlayer correlated states²⁻⁷. Here we report interlayer drag measurements between graphene and superconducting LaAlO₃/SrTiO₃ (LAO/STO) heterointerface separated by a natural insulating barrier of LAO (as thin as 2 nm). Applying a drive current (I_{drive}) in the graphene layer induces a negative drag voltage at the LAO/STO interface in the vicinity of the superconducting transition, which is attributed to the supercurrent drag effect, arising from the interlayer interactions involving the superconducting carriers. Benefiting from the high tunability of both layers and the ultra-small interlayer spacing, an extremely large interlayer current coupling ratio ($r = |I_{\text{drag}}/I_{\text{drive}}|$, I_{drag} : the equivalent drag current at LAO/STO interface) is eventually achieved, surpassing conventional systems consisting of normal metal and superconducting films by two orders of magnitude⁸. More strikingly, this ratio is estimated to be up to 10^5 at the zero-temperature limit. The unique temperature- and carrier density/polarity-dependent behaviors suggest a brand-new microscopic interaction mechanism accounting for the observed giant supercurrent drag effect. Our study is anticipated to inspire further exploration of hybrid interlayer coupling via utilization of newly-emerging two-dimensional electronic systems, in particular those exhibiting long-range electronic and magnetic orders.

The frictional drag effect is a transport phenomenon where moving charge carriers in one layer (drive layer) induce the transport of charge carriers in another layer (drag layer) via interlayer interactions between two closely spaced but electrically isolated conductors¹. Drag experiments have been demonstrated to be an effective approach to detect elementary excitations⁹⁻¹¹, and moreover, to reveal novel correlated condensate states, such as the even-denominator fractional quantum Hall state^{3,4} and the excitonic superfluidity⁵⁻⁷. It is thus natural to consider replacing one of the conducting layers with a superconductor. In such a hybrid structure, drag measurement has been theoretically demonstrated to be an alternative way to reveal the order parameters fluctuations in the superconducting (SC) layer¹²⁻¹⁴. More importantly, the interactions between the normal and SC carriers may give rise to unique interlayer coupling effects, such as the non-dissipative drag effect¹⁵, which was originally proposed to exist in ³He-⁴He mixtures¹⁶ and neutron stars¹⁷. Preliminary experimental investigations using double-layer electronic systems consisting of normal metal and SC films were conducted over two decades ago^{8,18}, wherein rather weak and uncontrolled drag responses were observed in the immediate vicinity of the SC transition.

Recent progress in the development of graphene and other two-dimensional (2D) electronic systems has sparked renewed interest in the study of interlayer interactions based on vertical 2D heterostructures¹⁹⁻²¹. Especially, the highly tunable electronic properties of component layers, together with the accessibility of ultra-small interlayer separation, enable the investigation of the drag effect in previously inaccessible regimes, and moreover, the discovery of a spectrum of novel interaction phenomena¹⁹⁻²⁵. In this study, a unique hybrid structure consisting of graphene and LaAlO₃/SrTiO₃ (LAO/STO) heterointerface is utilized to exploit the nontrivial interactions between a normal conductor and a superconductor at the ultimate 2D limit, in which a giant and highly tunable supercurrent drag effect is observed.

The schematic of the hybrid device comprising graphene and LaAlO₃/SrTiO₃, denoted as G-LAO/STO, is depicted in Fig. 1a. Macro-scale graphene (~2 mm) grown via chemical vapor deposition was used to avoid nanofabrication-induced degradation in the electronic performance of the LAO/STO interface (Fig. 1b, see Methods for the fabrication details). The pristine 2D superconductivity of the LAO/STO interface is well maintained in the final device, manifesting as the observation of a typical Berezinskii-Kosterlitz-Thouless (BKT) transition²⁶ (see Extended Data Fig. 1 and Supplementary Note

1 for details). Furthermore, the interfacial superconductivity of LAO/STO can be readily tuned using a back-gate voltage (V_{BG}) applied across the STO substrate (Fig. 1d), as similarly demonstrated in previous studies^{27,28}. The impact of V_{BG} on the doping level of graphene is negligible (Extended Data Fig. 2), demonstrating a perfect shielding effect of the LAO/STO layer. On the other hand, both the carrier type and density of the graphene layer can be tuned via the interlayer-gate voltage (V_{int}) utilizing LAO as the dielectric layer (Fig. 1c), with negligible impact on the electronic performance of the LAO/STO interface (Extended Data Fig. 3).

Before exploring the interlayer drag effect, we would like to note that from the temperature-dependent resistance (R - T) curves across the SC transition region of the LAO/STO interface (Fig. 1d), two-step resistance drops are clearly seen as a function of decreasing temperature. Such features can be better resolved from the second derivative of the R - T curves (Fig. 1e), where two characteristic temperatures, i.e. T_{P} and T_{F} , can be identified from the peaks. This observation, which has been reported in previous studies^{26,28}, can be rationalized in the context of electronic phase separation. In fact, both direct imaging and transport measurements have demonstrated that the 2D superconductivity at the LAO/STO interface is spatially inhomogeneous, manifesting as the disorder-induced formation of SC puddles, which results in patchy superfluid density with a typical length scale of micrometers^{29,30}. The ground state of the LAO/STO interface can be well interpreted as a Josephson junction array^{30,31}, where the inter-puddle Josephson coupling plays an essential role in the formation of global phase coherence. Within this scenario, the first resistance drop at T_{P} can be explained as the onset of electron pairing and thus the formation of local SC puddles, while the second resistance drop at T_{F} corresponds to the onset of inter-puddle phase coupling impaired by quantum fluctuations. Accordingly, four distinct states can be distinguished from the low-temperature phase diagram shown in Fig. 1f: the normal state, the local SC puddle state, the phase fluctuating state, and the global phase coherent 2D SC state (as schematically shown in Fig. 1g)²⁸. Notably, the three corresponding critical temperatures, T_{P} , T_{F} , and the SC transition temperature T_{C} , all exhibit a non-monotonic behavior with varying V_{BG} , and reach a maximum at nearly the same V_{BG} , corresponding to the optimal doping.

Following previous studies, the drag experiments were conducted by applying a drive current (I_{drive}) to the graphene layer and measuring the induced drag voltage (V_{drag}) at the LAO/STO interface^{1,19-21}. As schematically shown in Fig. 2a, the moving carriers in the graphene layer will result in a drag

current (I_{drag}) at the LAO/STO interface via interlayer interactions, and thus the accumulation of carriers at one end, which induces an open-circuit voltage that is readily measurable. Figure 2b depicts the obtained drag resistance ($R_{\text{drag}} = V_{\text{drag}}/I_{\text{drive}}$) as a function of T for Device #1 in which the interlayer spacer of the LAO layer is 5-unit-cell thick (~ 2 nm). The R - T curve of the LAO/STO interface is also plotted for comparison. It is clear that a negative drag signal occurs accompanying the SC transition of the LAO/STO interface, while there is no detectable drag signal when the LAO/STO interface is either in the normal or the fully SC state (see Extended Data Fig. 4-7 and Supplementary Note 2 for validity check). As a consequence, R_{drag} exhibits a non-monotonic dependence on temperature, reaching a maximum at $T \sim 195$ mK. These features, which are well reproduced in other G-LAO/STO devices (Extended Data Fig. 8), are not expected for the conventional Coulomb drag effect between carriers in the normal state¹. Applying a moderate in-plane magnetic field (B) of 1 T significantly depresses the superconductivity of the LAO/STO interface, manifesting as the broadening of the SC transition zone and the decrease of T_C (Fig. 2c). As for the drag effect, the temperature range for the non-zero drag signal broadens accordingly, and the peak of R_{drag} shifts towards lower temperatures (see also Fig. 2c). When the magnetic field is further increased to 3 T, the drag signal disappears with concomitant quenching of the LAO/STO interfacial superconductivity (see Extended Data Fig. 9 for results under the perpendicular field). The intimate correlation between the drag response and the SC transition of the LAO/STO interface is further evidenced from plots of R_{drag} vs B shown in Fig. 2d, where detectable drag voltage also occurs only within the SC transition region.

Such drag response is thus attributable to the supercurrent drag effect originated from the interlayer interactions involving the SC carriers^{8,15}. In this framework, the observed non-monotonic temperature dependent behavior of R_{drag} can be qualitatively understood as follows: when the LAO/STO interface is in the normal state, no drag response is detected, because the drag effect arising from the mutual Coulomb scattering between normal carriers is negligible at such low temperatures¹. With decreasing temperature, the emergence of SC carriers, which carry electric current without dissipation, will substantially enhance the interlayer drag response, leading to the occurrence of supercurrent drag effect. The as-induced drag current I_{drag} should increase continuously with decreasing temperature and eventually saturate when the LAO/STO interface reaches the fully SC state. Practically, we can only measure V_{drag} and thus R_{drag} ($V_{\text{drag}}/I_{\text{drive}}$), instead of I_{drag} , as detailed in Supplementary Note 3. The

competition between increasing I_{drag} and decreasing $R_{\text{LAO/STO}}$ with decreasing temperature in the SC transition region leads to the observed non-monotonic behavior of V_{drag} (expressed as $I_{\text{drag}} R_{\text{LAO/STO}}$) and thus R_{drag} . When the LAO/STO interface enters into the fully SC state, $R_{\text{LAO/STO}} = 0$, and thus R_{drag} vanishes again. In this supercurrent drag picture, applying magnetic field will suppress the SC state and therefore suppress the drag effect, which is indeed experimentally observed, as shown in Fig. 2c,d.

The high tunability of LAO/STO interfacial superconductivity enables investigation of the supercurrent drag effect in a wide-parameter space. Figure 3a shows the phase diagram of $R_{\text{LAO/STO}}$ obtained via sweeping V_{BG} at different T . A SC dome with a maximum $T_{\text{C}} \approx 180$ mK at $V_{\text{BG}} \sim 27$ V is clearly seen, which is in good agreement with previous studies^{27,28}. Next, systematic drag measurements were conducted to obtain the phase diagram of R_{drag} as functions of V_{BG} and T . As clearly shown in Fig. 3b, the regions where R_{drag} is non-zero also constitute a dome-like shape with respect to V_{BG} . The maximum R_{drag} could reach up to $\sim 2 \Omega$, much larger than those obtained in conventional systems consisting of normal metal and SC films^{8,18}. Similar consistency can also be seen via comparing the $V_{\text{BG}}-B$ phase diagrams of $R_{\text{LAO/STO}}$ and of R_{drag} , as demonstrated in Fig. 3d and Fig. 3e, respectively. These observations suggest that the interlayer drag effect can be utilized as a remote probe to unveil the SC properties.

More strikingly, when the extracted curves of T_{F} and T_{C} with respect to V_{BG} are overlaid with the phase diagram of R_{drag} in Fig. 3b, we found that the drag signal can be detected only when the temperature is below T_{F} in the whole V_{BG} range. That is, the supercurrent drag effect is getting enhanced to be detectable only when the inter-puddle SC phase coupling arises in the LAO/STO interface. When the temperature is below T_{C} , the measured R_{drag} become negligible since $R_{\text{LAO/STO}} \sim 0$, as discussed earlier.

Next, we sought to adopt the concept of current coupling ratio (in which $r = |I_{\text{drag}}/I_{\text{drive}}|$)^{8,15} to quantitatively characterize the supercurrent drag effect. Since $I_{\text{drag}} = V_{\text{drag}}/R_{\text{LAO/STO}}$, and $R_{\text{drag}} = V_{\text{drag}}/I_{\text{drive}}$, r can be expressed as $|R_{\text{drag}}/R_{\text{LAO/STO}}|$. Accordingly, we can readily obtain the mapping of r as functions of V_{BG} and T from the mappings of $R_{\text{LAO/STO}}$ and of R_{drag} in Fig. 3a and Fig. 3b. The result is shown in Fig. 3c, from which a dome-shaped r versus V_{BG} profile is clearly seen. For a certain V_{BG} , r first increases monotonically with decreasing T , and then becomes unattainable upon reaching the fully SC state of the LAO/STO interface ($R_{\text{LAO/STO}} \sim 0$), where the absolute error approaches infinity.

Notably, the maximum value of r is ~ 0.3 at $V_{\text{BG}} \sim 20$ V and $T \sim 170$ mK. As a comparison, r is on the order of 10^{-3} in the previous study in which AlO_x and Au/Ti serve as the superconductor and normal conductor layers, respectively⁸. The highly tunable and strong interlayer coupling is also clearly seen from the mapping of r as functions of V_{BG} and B shown in Fig. 3f, and can be reasonably attributed to two main advantages of the present G-LAO/STO device: the ultra-small interlayer spacing, and the spatially uniform interlayer interactions. In addition, the relatively low carrier densities of graphene (LAO/STO interface) compared to a normal metal (SC film) leads to a reduced screening effect on the interlayer interactions, which may also contribute to the giant supercurrent drag effect.

For the experimentally attainable regime, r increases with decreasing temperature, consistent with the enhanced superconductivity of the LAO/STO interface. It is of note that in a homogeneous superconductor the superfluid density (n_s) also increases monotonically with decreasing temperature, obeying a phenomenological BCS model $n_s = n_0[1-(T/T_{\text{SC}})^b]$, where n_0 is the superfluid density at absolute zero, T_{SC} is the temperature where Cooper pairs start to emerge, and b is a parameter describing how rapidly the gap opens below T_{SC} ³². It is reasonable to assume that the strength of drag effect, and thus r is determined by the magnitude of n_s ⁸. Considering LAO/STO is a s-wave superconductor and $b = 2$ ^{31,33}, we used the equation $r = r_0[1-(T/T^*)^2]$ in an attempt to fit the r vs T curve, where r_0 represents the current coupling ratio at the zero-temperature limit, and T^* is a critical temperature. Figure 4a shows the typical result obtained at $V_{\text{BG}} = 0$ V, from which a clear deviation between the experimental and modeled data is seen, especially in the temperature region corresponding to the sharp increase of r . The inconsistency can be better seen from the semi-log plots shown in the inset of Fig. 4a, suggesting that other issues, such as the inhomogeneity of superconductivity, must be considered to give a more quantitative description.

As discussed above, the LAO/STO interface has been widely recognized as a superconductor possessing electronic phase separation. In the present G-LAO/STO device, detectable drag response can only be obtained at temperatures below T_{F} of the LAO/STO interface, corresponding to the emergence of inter-puddle Josephson coupling. Note that the inter-puddle Josephson coupling within the LAO/STO interface here is rooted in the SC proximity effect, i.e. the decay of the SC order parameters in the normal state region for an equivalent superconductor-normal-superconductor junction³⁴, while the interlayer supercurrent drag effect reflects the transport of SC carriers at the

LAO/STO interface induced by the moving normal carriers in the graphene layer. These characteristics imply the interlayer interaction strength should possess similar parameter-dependent behaviors with those of the inter-puddle Josephson coupling. It has been revealed that the inter-puddle Josephson coupling is proportional to $\exp(-T/a)$ (a is a parameter related to the normal-metal coherence length)³⁴⁻³⁷. Therefore the exponential term of $\exp(-T/a)$ is added in the right side of the equation $r = r_0[1-(T/T^*)^2]$ for further fitting of the r vs T curves, i.e. $r \sim r_0[1-(T/T^*)^2]\exp(-T/a)$, where a is a parameter that determines how rapidly the interlayer interaction strength increases with decreasing temperature.

The typical result from fitting using the modified equation is shown in Fig. 4a, from which excellent consistency between the experimental and the modeled data is evident (see Extended Data Fig. 11 for the results of another device). Moreover, the above formula agrees well with the experimental r vs T curves obtained at different V_{BG} (Fig. 4b). Accordingly, the ratio r at relatively low temperatures, which cannot be experimentally obtained as $R_{LAO/STO} \sim 0$, now can be reasonably estimated by using the above equation to fit the data. Strikingly, the extracted r_0 from the fitting also shows non-monotonic dependence with varying V_{BG} , and exceeds 10^5 for V_{BG} around the optimal doping (Fig. 4c). That is, at the zero-temperature limit, applying a drive current in a normal conductor can induce a striking 10^5 times larger secondary current in the superconductor layer in close proximity, demonstrating that such a giant drag effect may be utilized for developing novel SC electronic devices, e.g. current amplifier.

As for previous systems consisting of normal metal and SC films, different mechanisms of interlayer interactions have been proposed to explain the detected drag signal in the vicinity of the SC transition^{8,18}. One typical explanation is the Coulomb interactions between the carriers in the normal conductor and the Cooper pairs in the superconductor¹⁵. Since this model is based on the interlayer momentum transfer, the as-induced V_{drag} should be negative/positive when the carrier polarity in the two layers is the same/opposite^{1,19}. However, in the present study the measured V_{drag} is negative when the carrier types of the graphene layer and the LAO/STO interface are opposite, inconsistent with such a mere Coulomb interaction mechanism. An alternative explanation is the inductive coupling between the electrons in the normal conductor and the mobile vortices in the superconductor¹², in which the local fluctuating electric field induced by mobile vortices in the superconductor layer are considered to be the key factor. According to this mechanism, the drag signal should be always positive. Hence, it can also be readily excluded since the observed drag signal is always negative (also see Extended

Data Fig. 12). These analyses point to a brand-new interaction mechanism that will require more in-depth studies to be fully elucidated.

Last but not the least, the high tunability of the graphene layer permits additional experimental efforts that may offer more insight. As demonstrated in Extended Data Fig. 12, the drag signal remains negative upon tuning the graphene layer across the Dirac point, implying a carrier-polarity-independent microscopic origin. Besides, R_{drag} reaches the maximum when the Fermi level of the graphene layer is at the Dirac point, demonstrating the anti-correlations between the drag signal and the carrier density of the drive layer. Even though more research is still needed to nail down the intrinsic nature of the observed supercurrent drag effect, the revealed dependencies here will certainly place further substantive constraints on theoretical understandings. It is anticipated that our study will promote further investigation of hybrid interlayer coupling via adopting newly-emerging 2D electronic systems³⁸⁻⁴⁰, and thus the fundamental understanding of electronic frictional effects that is imperative to the future design of novel electronic devices.

References

- 1 Narozhny, B. & Levchenko, A. Coulomb drag. *Rev. Mod. Phys.* **88**, 025003 (2016).
- 2 Eisenstein, J. & MacDonald, A. H. Bose-Einstein condensation of excitons in bilayer electron systems. *Nature* **432**, 691-694 (2004).
- 3 Suen, Y., Engel, L., Santos, M., Shayegan, M. & Tsui, D. Observation of a $\nu=1/2$ fractional quantum Hall state in a double-layer electron system. *Phys. Rev. Lett.* **68**, 1379-1382 (1992).
- 4 Eisenstein, J., Boebinger, G., Pfeiffer, L., West, K. & He, S. New fractional quantum Hall state in double-layer two-dimensional electron systems. *Phys. Rev. Lett.* **68**, 1383-1386 (1992).
- 5 Kellogg, M., Eisenstein, J., Pfeiffer, L. & West, K. Vanishing Hall resistance at high magnetic field in a double-layer two-dimensional electron system. *Phys. Rev. Lett.* **93**, 036801 (2004).
- 6 Tutuc, E., Shayegan, M. & Huse, D. A. Counterflow measurements in strongly correlated GaAs hole bilayers: evidence for electron-hole pairing. *Phys. Rev. Lett.* **93**, 036802 (2004).
- 7 Nandi, D., Finck, A. D. K., Eisenstein, J. P., Pfeiffer, L. N. & West, K. W. Exciton condensation and perfect Coulomb drag. *Nature* **488**, 481-484 (2012).
- 8 Huang, X., Bazàn, G. & Bernstein, G. H. Observation of supercurrent drag between normal metal and superconducting films. *Phys. Rev. Lett.* **74**, 4051-4054 (1995).
- 9 Yamamoto, M., Stopa, M., Tokura, Y., Hirayama, Y. & Tarucha, S. Negative Coulomb drag in a one-dimensional wire. *Science* **313**, 204-207 (2006).
- 10 Price, A., Savchenko, A., Narozhny, B., Allison, G. & Ritchie, D. Giant fluctuations of Coulomb drag in a bilayer system. *Science* **316**, 99-102 (2007).

- 11 Laroche, D., Gervais, G., Lilly, M. & Reno, J. 1D-1D Coulomb drag signature of a Luttinger liquid. *Science* **343**, 631-634 (2014).
- 12 Shimshoni, E. Role of vortices in the mutual coupling of superconducting and normal-metal films. *Phys. Rev. B* **51**, 9415-9418 (1995).
- 13 Zou, Y., Refael, G. & Yoon, J. Investigating the superconductor-insulator transition in thin films using drag resistance: Theoretical analysis of a proposed experiment. *Phys. Rev. B* **80**, 180503 (2009).
- 14 Levchenko, A. & Norman, M. R. Proposed Giaever transformer to probe the pseudogap phase of cuprates. *Phys. Rev. B* **83**, 100506 (2011).
- 15 Duan, J.-M. & Yip, S. Supercurrent drag via the Coulomb interaction. *Phys. Rev. Lett.* **70**, 3647-3650 (1993).
- 16 Andreev, A. & Bashkin, E. Three-velocity hydrodynamics of superfluid solutions. *Sov. Phys. JETP* **42**, 164-167 (1976).
- 17 Alpar, M., Langer, S. A. & Sauls, J. Rapid postglitch spin-up of the superfluid core in pulsars. *Astrophys. J.* **282**, 533-541 (1984).
- 18 Giordano, N. & Monnier, J. Cross-talk effects in superconductor-insulator-normal-metal trilayers. *Phys. Rev. B* **50**, 9363-9368 (1994).
- 19 Kim, S. *et al.* Coulomb drag of massless fermions in graphene. *Phys. Rev. B* **83**, 161401 (2011).
- 20 Gorbachev, R. *et al.* Strong Coulomb drag and broken symmetry in double-layer graphene. *Nat. Phys.* **8**, 896-901 (2012).
- 21 Gamucci, A. *et al.* Anomalous low-temperature Coulomb drag in graphene-GaAs heterostructures. *Nat. Commun.* **5**, 5824 (2014).
- 22 Liu, X., Watanabe, K., Taniguchi, T., Halperin, B. I. & Kim, P. Quantum Hall drag of exciton condensate in graphene. *Nat. Phys.* **13**, 746-750 (2017).
- 23 Li, J., Taniguchi, T., Watanabe, K., Hone, J. & Dean, C. Excitonic superfluid phase in double bilayer graphene. *Nat. Phys.* **13**, 751-755 (2017).
- 24 Liu, X. *et al.* Interlayer fractional quantum Hall effect in a coupled graphene double layer. *Nat. Phys.* **15**, 893-897 (2019).
- 25 Li, J. *et al.* Pairing states of composite fermions in double-layer graphene. *Nat. Phys.* **15**, 898-903 (2019).
- 26 Reyren, N. *et al.* Superconducting interfaces between insulating oxides. *Science* **317**, 1196-1199 (2007).
- 27 Caviglia, A. *et al.* Electric field control of the LaAlO₃/SrTiO₃ interface ground state. *Nature* **456**, 624-627 (2008).
- 28 Chen, Z. *et al.* Carrier density and disorder tuned superconductor-metal transition in a two-dimensional electron system. *Nat. Commun.* **9**, 4008 (2018).
- 29 Bert, J. A. *et al.* Direct imaging of the coexistence of ferromagnetism and superconductivity at the LaAlO₃/SrTiO₃ interface. *Nat. Phys.* **7**, 767-771 (2011).
- 30 Biscaras, J. *et al.* Multiple quantum criticality in a two-dimensional superconductor. *Nat. Mater.* **12**, 542-548 (2013).
- 31 Manca, N. *et al.* Bimodal phase diagram of the superfluid density in LaAlO₃/SrTiO₃ revealed by an interfacial waveguide resonator. *Phys. Rev. Lett.* **122**, 036801 (2019).
- 32 Prozorov, R. & Giannetta, R. W. Magnetic penetration depth in unconventional superconductors. *Supercon. Sci. Technol.* **19**, R41 (2006).

- 33 Bert, J. A. *et al.* Gate-tuned superfluid density at the superconducting LaAlO₃/SrTiO₃ interface. *Phys. Rev. B* **86**, 060503 (2012).
- 34 De Gennes, P. G. Boundary effects in superconductors. *Rev. Mod. Phys.* **36**, 225-237 (1964).
- 35 Abraham, D. W., Lobb, C., Tinkham, M. & Klapwijk, T. Resistive transition in two-dimensional arrays of superconducting weak links. *Phys. Rev. B* **26**, 5268-5271 (1982).
- 36 Lobb, C., Abraham, D. W. & Tinkham, M. Theoretical interpretation of resistive transition data from arrays of superconducting weak links. *Phys. Rev. B* **27**, 150-157 (1983).
- 37 Eley, S., Gopalakrishnan, S., Goldbart, P. M. & Mason, N. Approaching zero-temperature metallic states in mesoscopic superconductor-normal-superconductor arrays. *Nat. Phys.* **8**, 59-62 (2012).
- 38 Saito, Y., Nojima, T. & Iwasa, Y. Highly crystalline 2D superconductors. *Nat. Rev. Mater.* **2**, 16094 (2017).
- 39 Gong, C. & Zhang, X. Two-dimensional magnetic crystals and emergent heterostructure devices. *Science*, **363**, 6428 (2019).
- 40 Liu, H., Liu, W. E. & Culcer, D. Anomalous Hall Coulomb drag of massive Dirac fermions. *Phys. Rev. B*, **95**, 205435 (2017).

Methods

Device fabrication. LAO/STO heterostructures were fabricated using pulsed laser deposition following those described in our previous study⁴¹. The ultra-flat surface and the good interfacial conductivity were verified prior to the following procedures. Monolayer graphene sheets were grown on Cu foils by chemical vapor deposition⁴², and then transferred directly onto the LAO/STO surface as previously reported⁴³. For the transport measurements, Al (Au) wires were connected to the LAO/STO interface (the graphene layer) using ultrasonic welding (silver conductive paint). Ti/Au contacts with a thickness of 5/50 nm were fabricated on the back side of the STO substrates to apply the back-gate voltage.

Electronic transport measurements. The electronic transport measurements were performed in an Oxford Instruments Triton Dilution Refrigerator. During the drag measurements, direct current (DC) mode was adopted to avoid possible influence of capacitive reactance in alternating current (AC) measurements²⁰. Keithley 6220/6221 and 2182A were employed to supply the currents in the drive layer and measure the voltage drops in the drag layer, respectively. To eliminate the voltage background of 2182A, the current was applied using a bipolar mode, and the voltage was obtained by taking the average of the measured voltages at positive and negative currents.

- 41 Liang, H. *et al.* Nonmonotonically tunable Rashba spin-orbit coupling by multiple-band filling control in SrTiO₃-based interfacial d-electron gases. *Phys. Rev. B* **92**, 075309 (2015).
- 42 Li, X. *et al.* Large-area synthesis of high-quality and uniform graphene films on copper foils. *Science* **324**, 1312-1314 (2009).
- 43 Cheng, L. *et al.* Photoconductivity of graphene in proximity to LaAlO₃/SrTiO₃ heterostructures: phenomenon and photosensor applications. *Phys. Rev. Appl.* **6**, 014005 (2016).

Acknowledgments

This work was supported by the Strategic Priority Research Program of Chinese Academy of Sciences (Grant No. XDC07010000), the National Natural Science Foundation of China (Grant Nos. 11974324, 11804326, U1832151), the National Key Research and Development Program of China (Grant No. 2017YFA0403600), the Anhui Initiative in Quantum Information Technologies (Grant No. AHY170000), and Hefei Science Center CAS (Grant No. 2020HSC-UE014). Part of this work was carried out at the USTC Center for Micro and Nanoscale Research and Fabrication.

Author contributions

C.Z. and L.L. conceived the project; R.T. and L.L. performed the experiments with assistance from L.G., X.F., L.Z. and Y.Y.; L.L., R.T. and C.Z. analyzed the data and wrote the manuscript; Z.Z. contributed to data interpretation and presentation. All authors contributed to the scientific discussion and manuscript revisions.

Competing financial interests

The authors declare no competing financial interests.

Figures

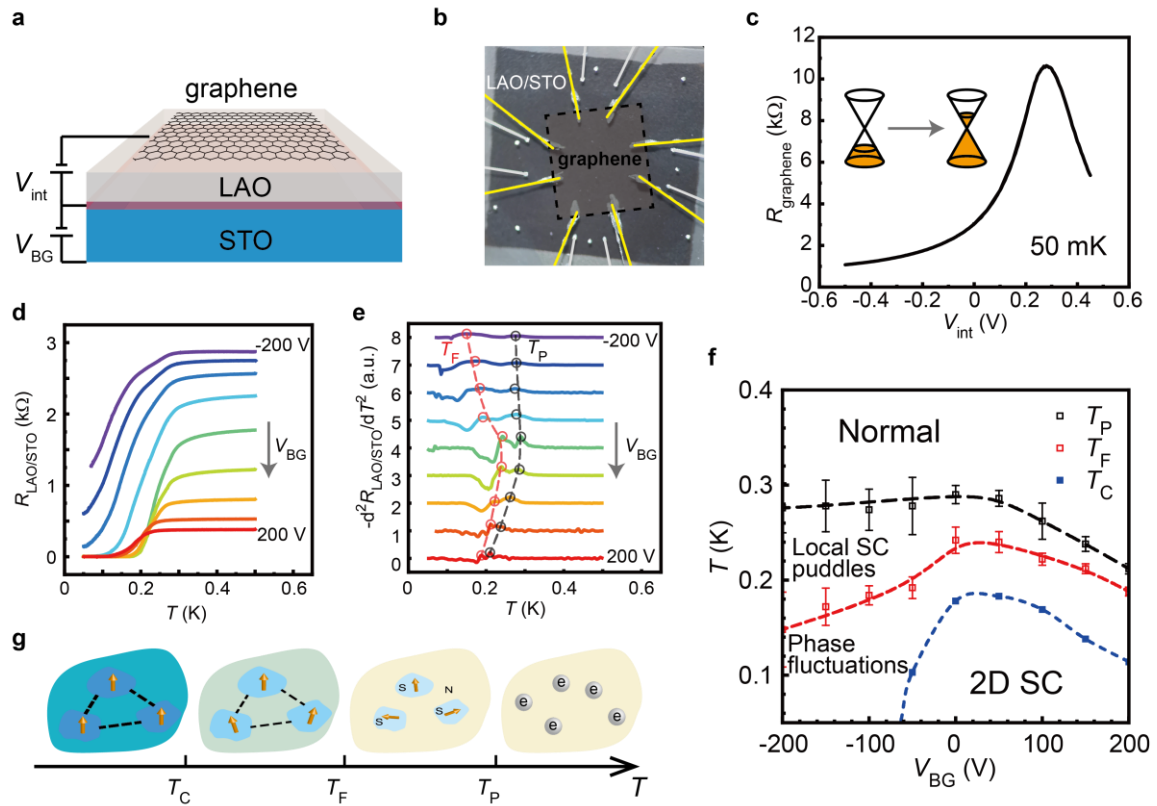


Figure 1 | Device and intralayer transport characterizations. **a**, Schematic illustration and **b**, optical microscope image of the G-LAO/STO device. **c**, Resistance of graphene (R_{graphene}) as a function of V_{int} measured at 50 mK. **d**, Resistance of the LAO/STO interface ($R_{\text{LAO/STO}}$) as a function of temperature (T) with V_{BG} varying from -200 to 200 V in increments of 50 V. **e**, Second derivative of the R - T curves shown in **d**. The two peaks denoted as T_F and T_P are tracked with red and black circles, respectively. **f**, Low-temperature phase diagram as functions of V_{BG} and T . Here, for simplicity, T_C (indicated with the dashed blue line) is defined as the temperature at which the resistance drops to 1% of the normal state resistance at $T = 400$ mK. T_F and T_P (indicated with the dashed black and red lines, respectively) are extracted from the second derivative peaks in **e**. The error bars are defined by the width of the peaks. **g**, Schematic illustration of the different states in the phase diagram shown in **f**.

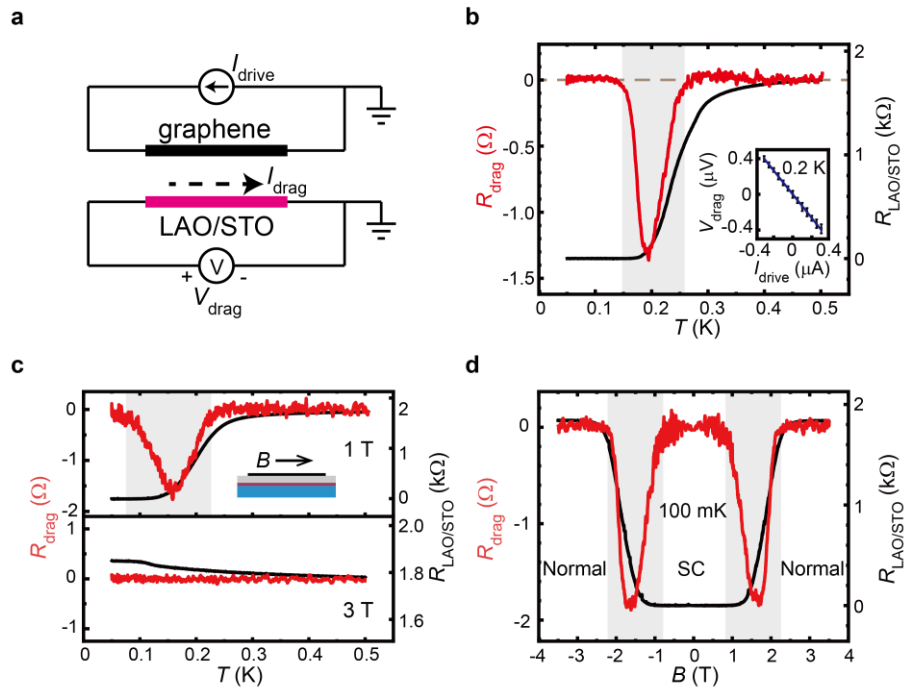


Figure 2 | Interlayer drag effect. **a**, Schematic illustration of the set-up for drag measurements. **b**, Drag resistance (R_{drag}) and $R_{\text{LAO/STO}}$ as a function of T . Inset: good linear dependence of measured V_{drag} at the LAO/STO interface upon applying I_{drive} at the graphene layer. **c**, T -dependent R_{drag} and $R_{\text{LAO/STO}}$ measured under 1 T and 3 T in-plane magnetic field, respectively. **d**, B -dependent R_{drag} and $R_{\text{LAO/STO}}$ measured at 100 mK. All the measurements were conducted at $V_{\text{BG}} = 0$.

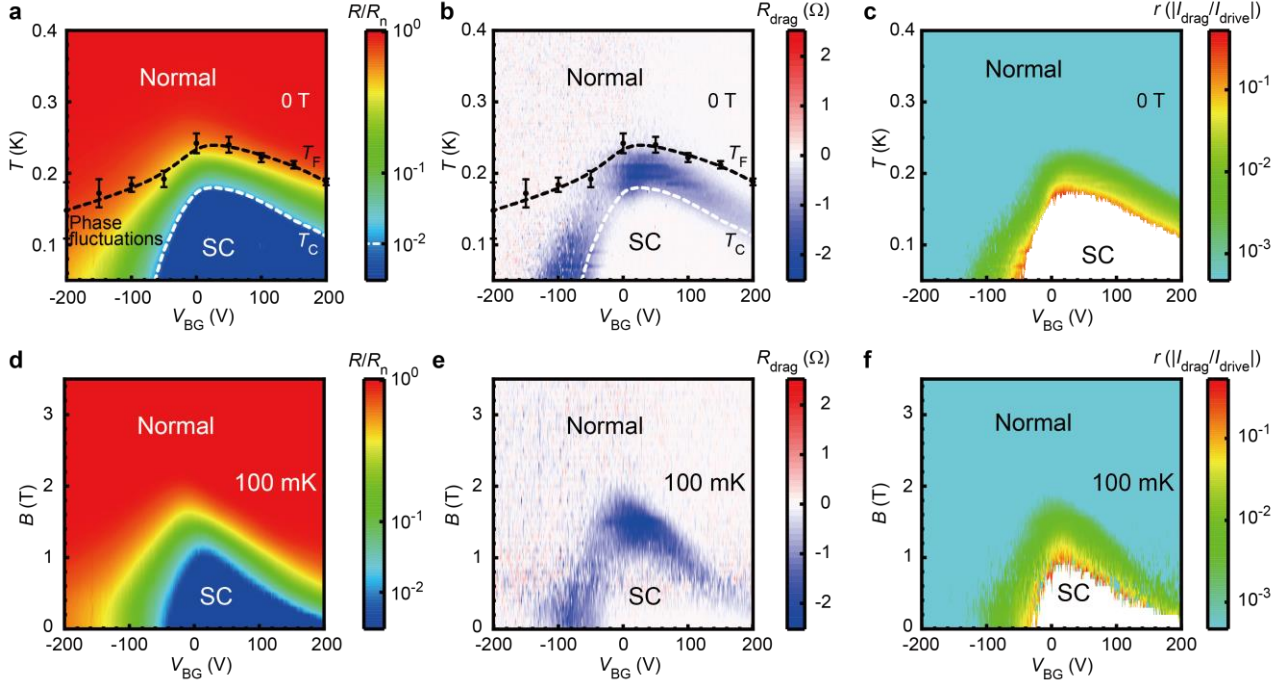


Figure 3 | Phase diagrams of the interlayer drag signal. **a-c**, Normalized resistance of the LAO/STO interface (R/R_n), R_{drag} , and interlayer current coupling ratio (r), as functions of V_{BG} and T , respectively. R_n is the normal state resistance of the LAO/STO interface at 400 mK measured under zero B . T_C (indicated by white dashed lines in **a** and **b**) is defined as the temperature at which $R/R_n=1\%$. **d-f**, R/R_n , R_{drag} , and r as functions of V_{BG} and the in-plane magnetic field B , respectively. The measurements were conducted at 100 mK.

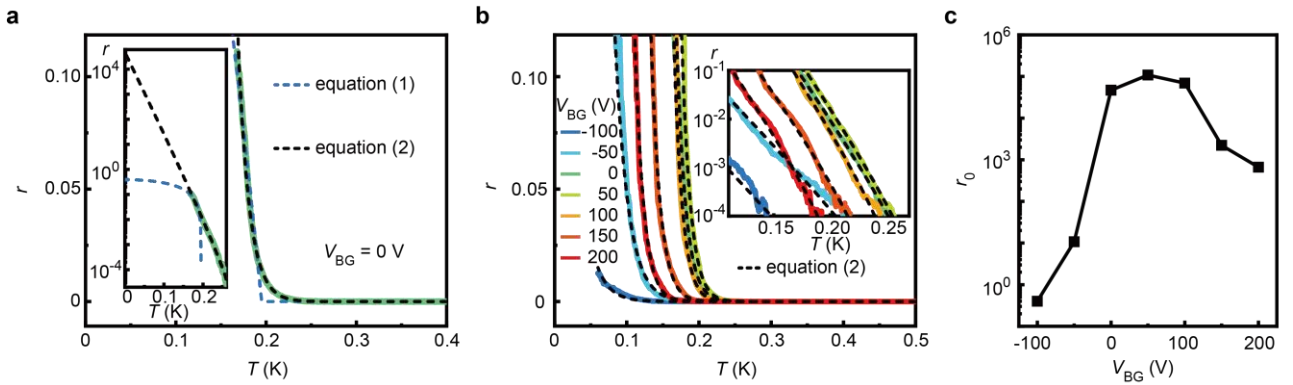


Figure 4 | Quantitative analysis on the interlayer current coupling ratio r . **a**, r as a function of T at $V_{\text{BG}} = 0$ V and the corresponding curves fitted using equation (1): $r = r_0[1-(T/T^*)^2]$ and equation (2): $r = r_0[1-(T/T^*)^2]\exp(-T/a)$. Inset: the semi-log plots for the low temperature region. **b**, r vs T for various V_{BG} . The black dashed lines are the curves fitted using equation (2). Inset: the corresponding semi-log plots. **c**, Extracted r_0 as a function of V_{BG} from the fittings in **b**.